Nanoscale

PAPER

View Article Online
View Journal | View Issue

Cite this: *Nanoscale*, 2025, **17**, 5328

Immobilization of horseradish peroxidase on UiO-66-NH$_2$ for colorimetric and fluorometric sensing of nitrite†

Zuyao Fu,[a] Lingfeng Yang,[a] Zhaoyang Ding *[a,b,c] and Jing Xie*[a,b]

Immobilized enzymes play a crucial role in analytical sensing due to their exceptional stability and considerable commercial importance. In this study, a stable Zr-based metal–organic framework (UiO-66-NH$_2$) was prepared as an immobilization platform for horseradish peroxidase (HRP) through covalent binding. HRP@UiO-66-NH$_2$ retained 75% of its activity after 10 cycles. Subsequently, a colorimetric/fluorometric dual-mode sensing strategy using HRP@UiO-66-NH$_2$ was developed for nitrite detection. HRP@UiO-66-NH$_2$ facilitated the transformation of the non-colored compound 3,3′,5,5′-tetramethylbenzidine (TMB) into its blue oxidized form. When nitrite is added, oxidized TMB (ox-TMB) specifically engaged with nitrite (NO_2^-) to generate diazotized TMB, leading to a color shift from blue to yellow. Concurrently, NO_2^- reacted with the amino groups of HRP@UiO-66-NH$_2$, forming diazonium compounds and suppressing the fluorescence of HRP@UiO-66-NH$_2$. The limits of detection were 0.21 μM and 0.19 μM for the colorimetric and fluorometric strategies, respectively. Furthermore, a portable kit for detecting nitrite was created by integrating gelatin with HRP@UiO-66-NH$_2$. The kit could visually identify nitrite from 10–400 μM in colorimetric mode and 0–400 μM in fluorometric mode. This method provides an innovative approach for nitrite sensing, paving the way for new research into multifunctional immobilized enzymes and their potential uses in biochemical sensing applications.

Received 29th November 2024,
Accepted 20th January 2025

DOI: 10.1039/d4nr05024j

rsc.li/nanoscale

1 Introduction

Enzymes are indispensable catalysts in living organisms, facilitating a myriad of reactions such as oxidation and decomposition.[1–3] Due to their high catalytic efficiency and excellent specificity, enzymes are widely utilized in the food industry, drug synthesis, analysis and sensing. However, their application is significantly restricted by the inherent sensitivity of protein molecules to high temperatures and extreme pH conditions. Moreover, the high cost associated with the non-reusability of enzymes is a major factor impeding the progress of various enzyme-based technologies.[4] One effective method for overcoming these constraints is to immobilize enzymes on a solid carrier. Immobilizing enzymes not only increases their stability under hard conditions and enables their repeated usage, but it can also enhance their catalytic activity if the right immobilization method and carrier are used.[5,6]

With advancements in enzyme immobilization technology, researchers have developed an increasing variety of materials for this purpose, including hydrogels,[7] mesoporous silica,[8] and metal–organic frameworks (MOFs).[9] The selection of an appropriate carrier is crucial for the design of immobilized enzyme systems.[10] Constructed by coordinating transition metal ions with organic ligands, MOFs are celebrated for their crystalline structure and significant porosity.[11] They offer significant surface areas, adjustable structures, and high porosity, making them ideal for applications in catalysis, gas separation, and pollutant adsorption. MOFs have unique properties, such as excellent biocatalytic performance, which make them have broad application prospects in biosensing, biocatalysis, biomedical imaging, and therapy.[12,13] Following the first preparation of enzyme@MOF composites,[14] an expanding community of scientists is showing growing interest in MOFs for their applications in enzyme immobilization. Studies have shown that the immobilization of enzyme protein molecules on MOFs can effectively improve enzyme activity, reusability, storage, chemical and thermal stability, and affinity for substrates.[15] By carefully selecting and designing MOFs, enzymes can maintain their original characteristics, such as a high level of catalytic efficiency, while also acquiring additional capabili-

---

[a] *College of Food Science and Technology, Shanghai Ocean University, Shanghai 201306, China. E-mail: zyding@shou.edu.cn, jxie@shou.edu.cn*

[b] *Shanghai Engineering Research Center of Aquatic-Product Processing & Preservation, Shanghai 201306, China*

[c] *Marine Biomedical Science and Technology Innovation Platform of Lin-gang Special Area, Shanghai 201306, China*

† Electronic supplementary information (ESI) available. See DOI: **https://doi.org/10.1039/d4nr05024j**

ties. Zr-MOFs, known for their large specific surface area and excellent fluorescence properties, were utilized to encapsulate glucose oxidase (GOx). This encapsulation preserved the high catalytic activity of GOx while also imparting fluorescence functionality. Consequently, a dual-functional detection platform was constructed, capable of detecting deoxynivalenol through both colorimetric and fluorescence methods.[16] Enzymes immobilized within MOFs exhibit catalytic properties that enhance signal amplification, making them suitable for use in biochemical detection, environmental surveillance, and the analysis of food products.[17]

Over the decades, nitrites, a class of nitrogen-containing compounds that are commonly found in nature, have been extensively employed in food processing. This is due to their exceptional color-protective and antioxidant properties, as well as their capacity to impede microbial growth and reproduction. Additionally, they have a prolonged shelf life that extends the shelf life of foods.[18–20] However, an excess of nitrite in food can rapidly attach to hemoglobin, impairing their ability to carry oxygen, which leads to local hypoxia and methemoglobinemia, posing significant health risks.[21,22] Additionally, metabolites of nitrite can react with secondary amines, resulting in the production of harmful nitrosamines known for their carcinogenic and mutagenic properties.[23,24] The World Health Organization (WHO) has identified nitrite as a carcinogenic substance and set a maximum allowable level of 3.0 mg L^{-1} (about 65 μM) in drinking water.[25] Therefore, it is crucial to develop accurate, easy-to-use, and budget-friendly approaches for detecting nitrite to ensure food safety and promote human health.

Currently, the colorimetric method based on Griess test is favored among the methods for the detection of nitrite because of its rapid reaction and simplicity of operation.[26] Furthermore, additional detection techniques utilizing the Griess reaction have been devised, including amalgamation with gold nanoparticles or the creation of portable hydrogel sensors for nitrite detection.[27,28] Also, it has been shown that nitrite can react with ox-TMB to produce a diazotization reaction, causing a shift in the color signal.[29] As a result, many researchers have turned to nano-enzymes to catalyze the TMB reaction for the development of colorimetric sensors.[30–33] However, nanozyme design and synthesis often require more complex steps, such as the careful engineering of surface properties and catalytic mechanisms. Nanozymes often exhibit multiple enzymatic activities (*e.g.*, peroxidase, oxidase, and catalase-like), but their broad enzymatic scope can limit their effectiveness in sensor applications. In contrast, the single, highly specific enzymatic activity of HRP ensures better selectivity for the target analyte, thereby improving the sensor's overall performance and reliability.

Some researchers have discovered that nitrite can react with the amino groups on the surface of UiO-66-NH_2 under acidic conditions, leading to the quenching of the fluorescence of UiO-66-NH_2.[34] This finding has enabled the development of fluorescence sensors for nitrite detection. Nevertheless, the majority of these methods are based on a single signal change in colorimetry or fluorescence, making them prone to environmental interference and limiting their sensitivity for detecting low concentrations.[35] Compared to the conventional single-signal detection methodology, multi-modal detection is seen to be a more promising method. Multi-modal detection is capable of satisfying the intricate detection requirements of daily life, while different signals can be verified against each other. Thus, multimodal detection can increase the range of applications as well as the sensitivity and accuracy of detection. However, developing a successful approach for multimodal detection of various analytes continues to be a significant barrier.[36]

Inspired by the views expressed above, a novel dual-mode sensor combining colorimetric and fluorometric techniques was created to quantify nitrite in complex samples. Through a simple solvothermal process, UiO-66-NH_2 was synthesized to exhibit strong fluorescence and stability, and then HRP was co-valently immobilized onto the UiO-66-NH_2 surface. As expected, HRP@UiO-66-NH_2 has inherently efficient catalytic activity, tunable photoluminescence properties, and good stability. HRP@UiO-66-NH_2 not only catalyzes the oxidation of colorless TMB to blue ox-TMB, but also exhibits blue fluorescence emission at 410 nm. Upon the introduction of nitrite, ox-TMB specifically interacts with it, producing diazotized TMB, which causes a progressive color transition from blue to green and ultimately to yellow (Scheme 1B). Additionally, nitrite reacts with the amino groups on UiO-66-NH_2 through a diazotization reaction, causing a rapid decrease in the fluorescence of UiO-66-NH_2. By leveraging the NO_2^- induced alterations in both colorimetric and fluorescent signals, nitrite was measured with high sensitivity, selectivity, reliability, and practicality through a dual-mode sensing approach. Furthermore, a portable kit for nitrite detection was created by embedding HRP@UiO-66-NH_2 into a gelatin hydrogel matrix. The kit enabled rapid on-site detection of nitrite. Thus, this study provided important enzyme@MOF nanocomposites for quantitative visual detection of NO_2^-.

2 Experimental procedure

2.1 Materials

Horseradish peroxidase (HRP), zirconium chloride ($ZrCl_4$), 2-amino-terephthalic acid, 3,3′,5,5′-tetramethylbenzidine (TMB), acetic acid (HAc), sodium acetate (NaAc), sodium nitrite ($NaNO_2$), *N*,*N*-dimethylformamide (DMF), anhydrous ethanol, sodium hydroxide, fluorescein isothiocyanate (FITC), *N*-hydroxy succinimide (NHS) and 1-(3-dimethylaminopropyl)-3-ethylcarbodiimide (EDC) were purchased from Aladdin (Shanghai, China) and used without further purification. Ultrapure water was used throughout the study.

2.2 Preparation of UiO-66-NH_2

A slightly modified solvothermal method was used for the preparation of UiO-66-NH_2.[37] First, $ZrCl_4$ (0.1 mM, 10 mL) was added dropwise to 2-aminoterephthalic acid solution (0.2 mM, 10 mL) under stirring conditions, and it was ensured that the dropwise addition process was completed in 30 min. Notably,

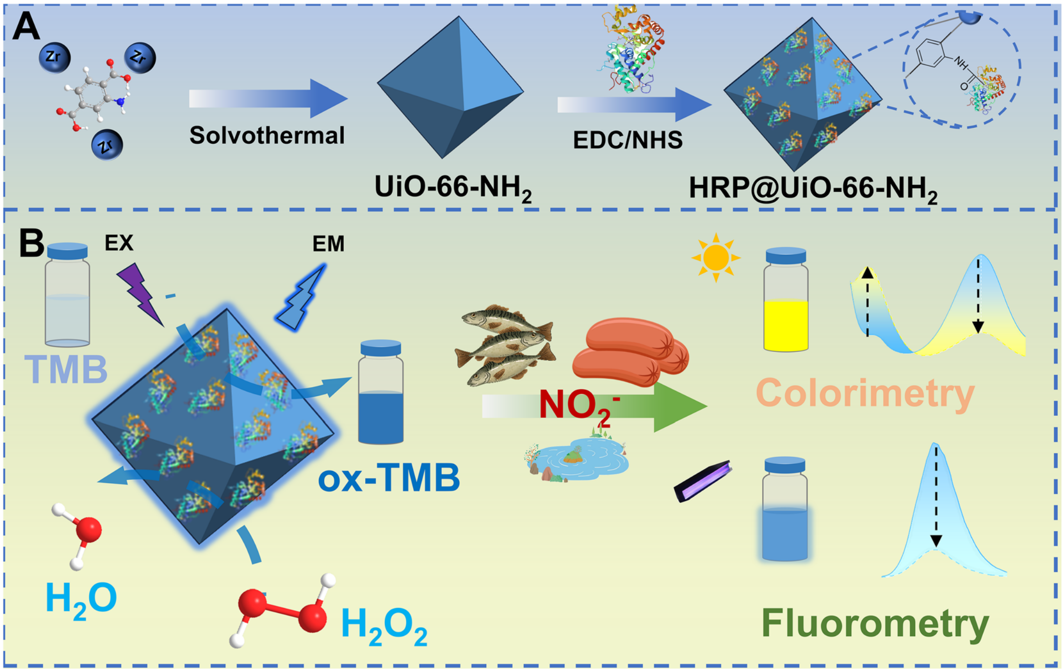

Scheme 1 (A) Schematic diagram for the preparation of HRP@UiO-66-NH$_2$; (B) illustration of the colorimetric/fluorometric detection of nitrite based on HRP@UiO-66-NH$_2$.

450 μL HAc was added to the 2-aminoterephthalic acid solution as a conditioner prior to the above steps. The mixture was maintained at 120 °C with stirring for 30 minutes and then continuously heated for 12 hours, resulting in a gradual turbidity of the solution. Afterward, the mixture underwent centrifugation at 12 000 rpm for 20 min to collect the precipitate, which was then washed three times with anhydrous ethanol. Finally, to acquire UiO-66-NH$_2$, the precipitate was completely dried in an oven at 75 °C.

2.3 Synthesis of HRP@ UiO-66-NH$_2$

HRP was immobilized on UiO-66-NH$_2$ as follows. HRP was dissolved in 2-(4-morpholino) ethanesulfonic acid buffer (0.1 M, pH 6.0) and then mixed with 10 mg of EDC. The mixture was incubated at room temperature with constant stirring for 1 h. Subsequently, 10 mg of NHS was added to the solution, and the incubation was continued for an additional 1.5 h. A solution containing 50 mg of UiO-66-NH$_2$ was prepared by dispersing it in 10 ml of phosphate-buffered saline (PBS, 0.01 mM, pH 7.4) using sonication. The activated HRP solution was then added to this solution, which was incubated overnight at room temperature. The resulting mixture was centrifuged at 12 000 rpm for 20 min to collect the precipitate and washed three times with PBS (0.05 mM, pH 7.4). The resulting precipitate was resuspended in 20 ml of PBS (0.01 mM, pH 7.4) and stored at 4 °C in the dark.

2.4 Quantification of the encapsulated enzymes in UiO-66-NH$_2$

Enzyme immobilization efficiency is expressed as the ratio of the mass of enzyme immobilized on UiO-66-NH$_2$ to the total mass of the original enzyme, represented as a percentage. Following enzyme immobilization, the enzyme concentration in the supernatant was measured with the Bradford assay.[38] In a typical procedure, 20 μL of the sample was placed in a 96-well microplate, and then 200 μL of Brilliant Blue G-250 reagent was added. After 5 min of reaction, the absorbance at 595 nm was measured.

2.5 Intrinsic fluorescence and peroxidase-mimetic catalytic activity of HRP@ UiO-66-NH$_2$

To observe the intrinsic fluorescence properties of HRP@ UiO-66-NH$_2$, 60 μL of HRP@UiO-66-NH$_2$ solution (0.1 mg mL^{-1}) was added to 2.94 mL NaAc–HAc solution (0.2 M, pH 4.0), and the fluorescence spectrum was obtained using a fluorescence spectrophotometer. The catalytic behavior of HRP@UiO-66-NH$_2$, mimicking peroxidase, was examined in a hydrogen peroxide solution using TMB as the color-generating substrate. In summary, 60 μL of HRP@UiO-66-NH$_2$ solution (0.1 mg mL^{-1}), 150 μL of H$_2$O$_2$ (100 mM), and 150 μL of TMB (5 mM) were mixed with 2.64 mL of NaAc–HAc buffer (0.2 M, pH 4.0). Following a 20-minute incubation, the absorbance was recorded with a UV-visible spectrophotometer. The fluorescence spectra were also measured for comparison with HRP@UiO-66-NH$_2$.

Enzymatic kinetic studies were conducted to assess the efficacy of the immobilized HRP. The affinity of the enzyme for the substrate is typically reflected in the K_m. Enzymatic kinetic studies were performed under the optimal conditions. First, the concentration of H$_2$O$_2$ was held constant, and the concentration of TMB, another substrate, was varied. The solution containing H$_2$O$_2$, HRP@UiO-66-NH$_2$, NaAc–HAc buffer, and varying TMB concentrations was incubated under specified conditions. The absorbance of this reaction mixture was tracked at 652 nm every 30 seconds for a duration of 5 minutes. Similarly, the dependence of the catalytic activity of HRP@UiO-66-NH_2 on the H_2O_2 concentration was determined by varying the H_2O_2 concentration and fixing the TMB concentration.

The K_m was calculated using the Lineweaver–Burk double reciprocal equation:

$$\frac{1}{\nu} = \frac{K_m}{\nu_{max}[S]} + \frac{1}{\nu_{max}}$$

where ν denotes the initial reaction speed, V_{max} represents the peak reaction rate, K_m signifies the Michaelis constant, and [S] stands for the substrate concentration.

2.6 Colorimetric/fluorometric assay for nitrite discrimination

The effectiveness of the nitrite detection method, employing both colorimetric and fluorometric techniques, was validated using various aqueous samples with NO_2^- concentrations spanning 0 to 500 μM. Under optimal conditions, HRP@UiO-66-NH_2 solution (0.1 mg mL^{-1}, 60 μL), H_2O_2 (100 mM, 150 μL), and TMB (5 mM, 150 μL) were added to the NaAc–HAc solution (0.2 M, pH 4.0). After incubation for 20 min, different concentrations of the NO_2^- solution were added to the mixture for 15 min. Subsequently, the UV–vis absorption and fluorescence signals were measured.

2.7 Selectivity and resistance to interference of HRP@UiO-66-NH_2 sensor

The selectivity and immunity studies were conducted according to the following steps. In brief, NO_2^- and the chosen interfering ions were introduced into the prepared assay setup and incubated for 15 minutes. Both UV-visible and fluorescence spectra were measured to assess selectivity. The anti-interference study differs from the selectivity study only by recording the UV-visible and fluorescence spectra of solutions of mixtures of NO_2^- coexisting with the above interfering ions.

2.8 Application in real samples

The preparation of the pickled fish and sausage samples followed the guidelines outlined in the Chinese national standard (GB 5009.33-2016). Briefly, the samples were chopped, and 5 g of the sample was weighed into a 250 mL corked conical bottle. Subsequently, 12.5 mL of a 50 g L^{-1} borax solution was added to approximately 150 mL of water at 70 °C, thoroughly mixed, and boiled for 15 minutes. After cooling to room temperature, the extract was placed in a 200 mL volumetric flask, and then 5 mL of potassium ferrocyanide (106 g L^{-1}) and 5 mL of zinc acetate (220 g L^{-1}) were added. The bottle was then filled with distilled water to a total volume of 200 mL, shaken thoroughly, and left for 30 min. Finally, the insoluble impurities were filtered using filter paper. The remaining filtrate was collected after discarding the initial filtrate (30 mL). Pickle brine and lake water samples were passed through a 0.22 μm microporous membrane for filtration. Pickled fish, sausage and pickle brine were purchased from local supermarkets, and lake water samples were obtained from the Shanghai Ocean University Campus. The recoveries were determined by adding different concentrations of NO_2^- standard solutions (50 and 100 μM) to the sample solutions to be tested. All samples, with and without sodium NO_2^-, were analyzed using the procedure described in section 2.6.

2.9 Preparation of a portable test kit using HRP@UiO-66-NH_2 immobilized gelatin hydrogels

Gelatin powder (0.5 g) was dissolved in 10 ml of deionized water at 60 °C and stirred until completely melted. The gelatin solution was cooled to 40 °C and 10 mL of the sensor dispersion was added to the above solution and stirred thoroughly to ensure homogeneity. Then 150 μL of the solution was added to each well of a 96-well microtiter plate to create a gelatin mixture. The hydrogels were stored at 4 °C until future use.

3 Results and discussion

3.1 Characterization

The process of immobilization of HRP with UiO-66-NH_2 as a carrier is shown in Scheme 1. This procedure involved two steps: synthesizing UiO-66-NH_2 and immobilizing HRP onto the surface of UiO-66-NH_2. The morphological changes before and after immobilization of the enzyme on UiO-66-NH_2 were characterized through scanning electron microscopy (SEM) and transmission electron microscopy (TEM). According to SEM analysis, UiO-66-NH_2 exhibited an octahedral shape and uniformity, with particles around 50 nm in size (Fig. 1A). After the immobilization, HRP@UiO-66-NH_2 presented irregularly shaped, larger, and somewhat agglomerated particles (Fig. 1B). TEM analysis indicated that HRP@UiO-66-NH_2 exhibited a rougher surface texture than the smooth UiO-66-NH_2, with enzyme immobilization causing noticeable agglomeration (Fig. 1C and D). To further confirm the immobilization of HRP in UiO-66, HRP was labeled with FITC and the labeled enzyme was immobilized in UiO-66-NH_2 using the same method. The confocal laser scanning microscopy (CLSM) image (Fig. S1†) showed significant green fluorescence from FITC-HRP, providing further evidence of the successful co-immobilization of HRP.

The dynamic light scattering (DLS) results showed a size of about 137.1 nm for UiO-66-NH_2, while the size increased to 342.4 nm for HRP@UiO-66-NH_2, confirming that the enzyme was successfully attached to the UiO-66-NH_2 (Fig. 1F). It is possible that agglomeration of the nanoparticles occurred during the testing process, which led to larger particle sizes in the DLS results compared to those obtained by TEM. Additionally, energy dispersive spectroscopy (EDS) was employed to observe the elemental distributions on the surface of UiO-66-NH_2 and HRP@UiO-66-NH_2 microregions. The analysis indicated that the elements carbon, nitrogen, oxygen, and zirconium were evenly distributed across both

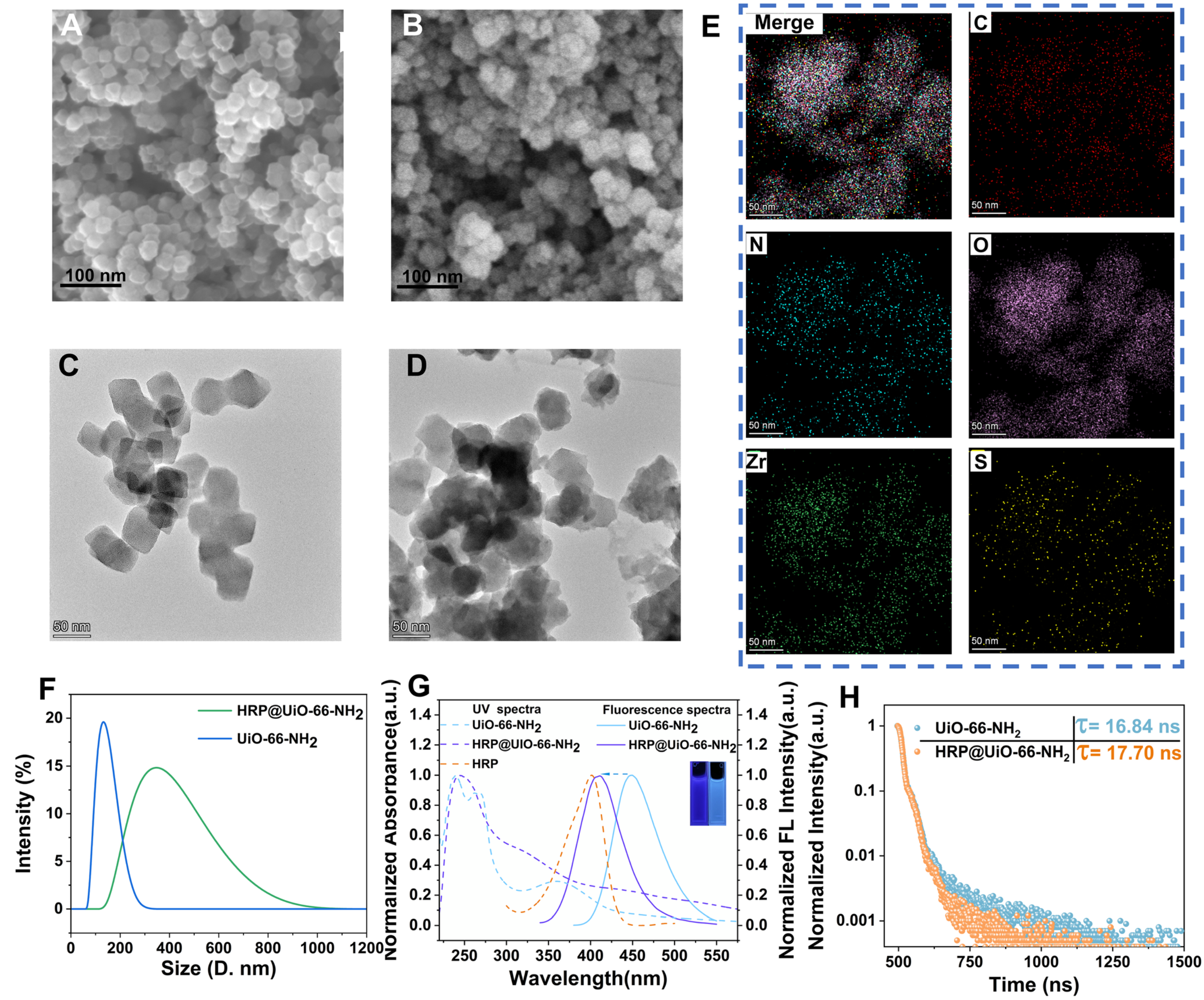

Fig. 1 Morphological characterization and fluorescence properties of UiO-66-NH_2 and HRP@UiO-66-NH_2. SEM images of (A) UiO-66-NH_2 and (B) HRP@UiO-66-NH_2. TEM images of (C) UiO-66-NH_2 and (D) HRP@UiO-66-NH_2. (E) Elemental mapping images of HRP@UiO-66-NH_2. (F) Size distribution comparison between UiO-66-NH_2 and HRP@UiO-66-NH_2. (G) UV absorption (solid lines) and fluorescence (dotted lines) spectra of UiO-66-NH_2 and HRP@UiO-66-NH_2. (H) Fluorescence lifetimes of UiO-66-NH_2 and HRP@UiO-66-NH_2.

materials, and the protein-specific element sulfur was also uniformly present in HRP@UiO-66-NH_2 (Fig. 1E). An increase in oxygen content from 23.86% to 80.15% further validated the effective attachment of the enzyme to UiO-66-NH_2 (Fig. S2 and 3†). Because HRP is a protein enzyme, its amino acid side chains, particularly those in serine, threonine, and tyrosine, contain a significant amount of oxygen.

Fig. 1G indicates that UiO-66-NH_2 showed a notable absorption peak at 360 nm; therefore, this wavelength was chosen for excitation purposes. Due to the absorption peak of HRP at 405 nm, the absorption of HRP@UiO-66-NH_2 at 360 nm was concealed. The fluorescence properties of UiO-66-NH_2 and HRP@UiO-66-NH_2 were compared by fluorescence emission spectroscopy. As shown in Fig. 1G, the fluorescence emission peak of HRP@UiO-66-NH_2 changed from 450 nm for UiO-66-NH_2 to 410 nm, and the fluorescence color changed from blue to blue-violet. The alteration of the fluorescence emission peak may be due to the interaction of HRP with the amino groups on UiO-66-NH_2, which affects its luminescence properties.[39] According to Fig. 1H, the fluorescence decay profiles of HRP@UiO-66-NH_2 and UiO-66-NH_2 displayed lifetimes of 16.84 ns and 17.70 ns, respectively, indicating minimal variation.

X-ray photoelectron spectroscopy (XPS) analysis of HRP@UiO-66-NH_2 identified elements such as C, N, O, Zr, Fe, and S, thereby confirming the effective synthesis of HRP@UiO-66-NH_2 (Fig. 2A). Elemental Fe and S were mainly derived from the ferrous ion center and disulfide bonds in the heme contained in HRP. However, because the HRP content is relatively low, the peaks corresponding to elemental Fe and S

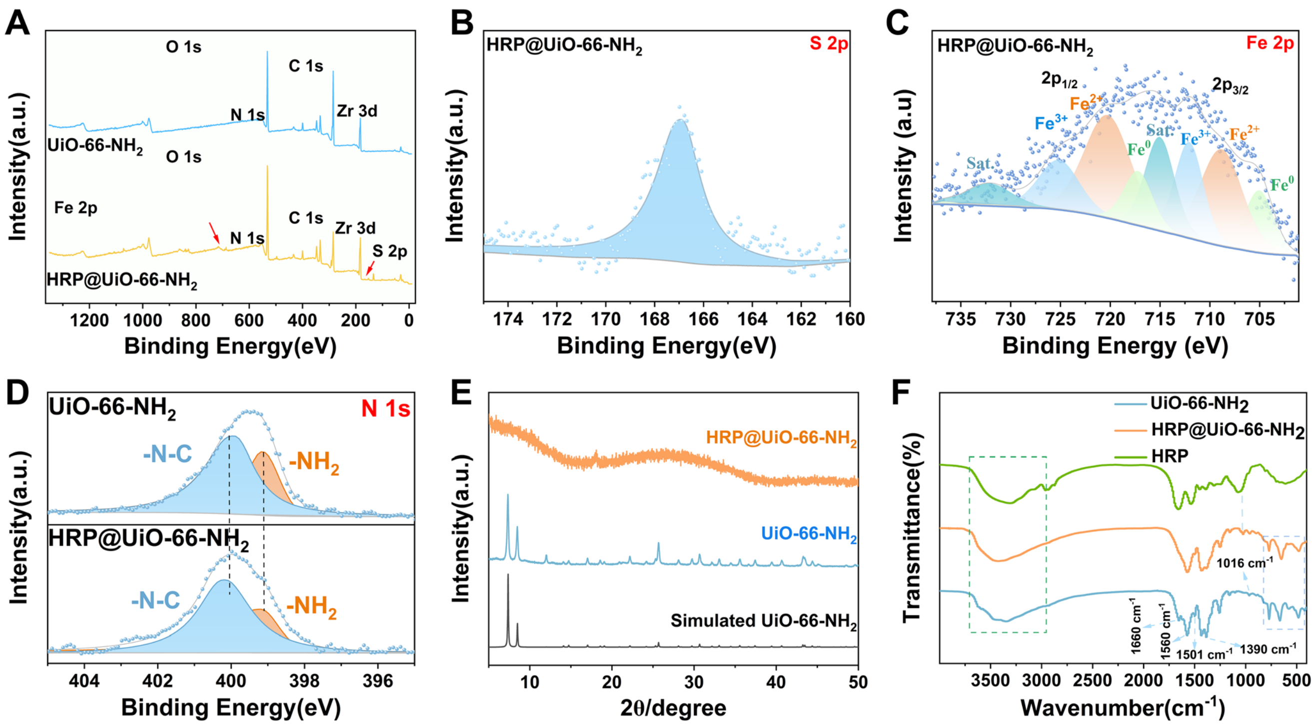

Fig. 2 Compositional analysis and structural characterization. (A) Survey XPS spectra of UiO-66-NH_2 and HRP@UiO-66-NH_2. (B) S 2p high-resolution XPS spectrum of HRP@UiO-66-NH_2. (C) Fe 2p high-resolution XPS spectrum of HRP@UiO-66-NH_2. (D) N 1s high-resolution XPS spectra of UiO-66-NH_2 (top) and HRP@UiO-66-NH_2 (bottom). (E) XRD patterns of UiO-66-NH_2 and HRP@UiO-66-NH_2. (F) FTIR spectra of UiO-66-NH_2 and HRP@UiO-66-NH_2.

in the survey XPS spectrum are not prominent. High-resolution maps of these elements were fitted using peak splitting to determine the valence and structure of each element. Within the C 1s spectrum of UiO-66-NH_2, peaks appearing at 284.80 eV, 285.90 eV, and 288.77 eV were identified and linked to the C–C, C–O–C, and O–C═O functional groups, respectively[40] (Fig. S6†). In addition, the peaks at 399.14 eV and 399.90 eV in Fig. 2D correspond to –NH_2 and –N–C, respectively.[41] At the same time, a decrease in the amount of –NH_2 can be seen. This may be due to the combination of HRP with the amino group on the surface of UiO-66-NH_2 to generate new amide bonds. The signals of O 1s at 531.83 eV, 533.33 eV, and 530.25 eV correspond to Zr–O–Zr, Zr–OH, and O–H, respectively[42] (Fig. S7†). The high-resolution profile of Zr 3d (Fig. S8†) splits into two asymmetric peaks located at 185.37 eV for Zr $3d_{3/2}$ and 182.93 eV for Zr $3d_{5/2}$.[43] In HRP@UiO-66-NH_2, the positions of the C, N, O, and Zr peaks showed some shifts relative to those observed in UiO-66-NH_2. Moreover, the valence state of Fe, as indicated by the high-resolution elemental mapping (Fig. 2C), is predominantly Fe^{2+}, aligning with the Fe state found in the active site of HRP. It also contains Fe^0 and Fe^{3+} to a lesser extent, which is probably due to the redox reactions of elemental Fe during immobilization or testing.

X-ray diffraction (XRD) was used to characterize the crystalline shapes of the prepared materials. The experimental and simulated XRD spectra show excellent agreement, confirming the successful synthesis of UiO-66-NH_2. The clear and defined peaks at 2θ values of 7.3°, 8.6°, and 25.7°, assigned to the (111), (200), and (531) planes, respectively, correspond to UiO-66-NH_2. These results are consistent with literature data, verifying the high crystallinity of the synthesized samples.[44] Following enzyme immobilization, only a single prominent peak at $2\theta = 25.7°$ was observed (Fig. 2E). This is partly attributed to the substantial enzyme coverage on the surface of UiO-66-NH_2, which obscured its signal, and partly to the agglomeration-induced shape change of UiO-66-NH_2, which decreased peak intensity. It is hypothesized that the interaction between HRP and UiO-66-NH_2 may induce localized structural distortion at the enzyme-binding sites, which could reduce the number of detectable crystallographic peaks. These results further confirm the successful synthesis of HRP@UiO-66-NH_2.

To further verify the successful synthesis of the prepared materials, Fourier transform infrared spectroscopy (FTIR) characterization of UiO-66-NH_2 and HRP@UiO-66-NH_2 was performed. The successful loading of the HRP enzyme was confirmed by the characteristic absorption peaks observed in HRP@UiO-66-NH_2, which correspond to both HRP and UiO-66-NH_2. The spectrum of UiO-66-NH_2 is shown in Fig. 2F, and the typical peak at 3340 cm^{-1} is due to the stretching vibration of the amino group. The signals observed at 1660 cm^{-1} were caused by the asymmetric stretching of C═O remaining in DMF. The bands observed at 1560 cm^{-1}, 1390 cm^{-1}, and 1501 cm^{-1} are attributed to the asymmetric and symmetric stretching of the carboxylate group in the ligand and the benzene ring vibrations, respectively.[45] The peak at 1016 cm^{-1} is due to the Zr–O single bond vibration in UiO-66-NH_2. The peaks between 800 and 500 cm^{-1} correspond to the in-plane and out-of-plane bending modes of the COO^- group.[46] The absorption peak of the amide I band in HRP at 3340 cm^{-1} is primarily attributed to N–H vibration, which also appears in UiO-66-NH_2. The absorption peak in the amide II band at 1660 cm^{-1}, attributed to C═O vibration, shifts to 1580 cm^{-1} after loading onto UiO-66-NH_2. However, this shifted peak overlaps with the absorption peak of UiO-66-NH_2.

The nitrogen adsorption isotherm technique was utilized to investigate the specific surface areas and pore structures of the synthesized samples. Fig. 3A illustrates that the specific surface area of UiO-66-NH_2 dropped significantly from 160.779 m^2 g^{-1} to 20.584 m^2 g^{-1} following the incorporation of HRP, indicating that the majority of the available voids were filled by enzyme molecules. The reduction in the BET specific surface area can be ascribed to the higher density of the material caused by enzyme immobilization and disruptions in crystallinity induced by the enzyme, confirming successful enzyme loading.[47] According to density functional theory (DFT) analysis, the pore size distribution of UiO-66-NH_2 showed minimal variation following enzyme immobilization, with values of 1.190 nm and 1.192 nm, respectively. This suggests that the HRP enzyme did not penetrate the interior of the UiO-66-NH_2 (Fig. 3B). The reduction in pore volume may be attributed to the HRP coating the surface of the UiO-66-NH_2, which obstructs a portion of its pore channels. Furthermore, zeta potential measurements of HRP, UiO-66-NH_2, and the immobilized enzyme revealed that the potentials of all three substances were negative, which ruled out the possibility that the enzyme was bound to the surface of UiO-66-NH_2 through electrostatic adsorption and this further indicated that the enzyme was bound to UiO-66-NH_2 through covalent bonding (Fig. 3C).

The results of thermogravimetric analysis (TGA) are presented in Fig. 3D. The thermal decomposition of free HRP occurred within the temperature range of 200 to 550 °C. HRP@UiO-66-NH_2 had a faster rate of weight loss than UiO-66-NH_2 in the 243–507 °C range attributed to the breakdown of the enzyme. The degradation rates of HRP@UiO-66-NH_2 and UiO-66-NH_2 differed significantly due to the enzyme loading. In the range of 500–800 °C both materials exhibited a fast rate of weight loss, which was due to the decomposition of the ligand in UiO-66-NH_2. TGA confirmed the successful incorporation of HRP into UiO-66-NH_2.

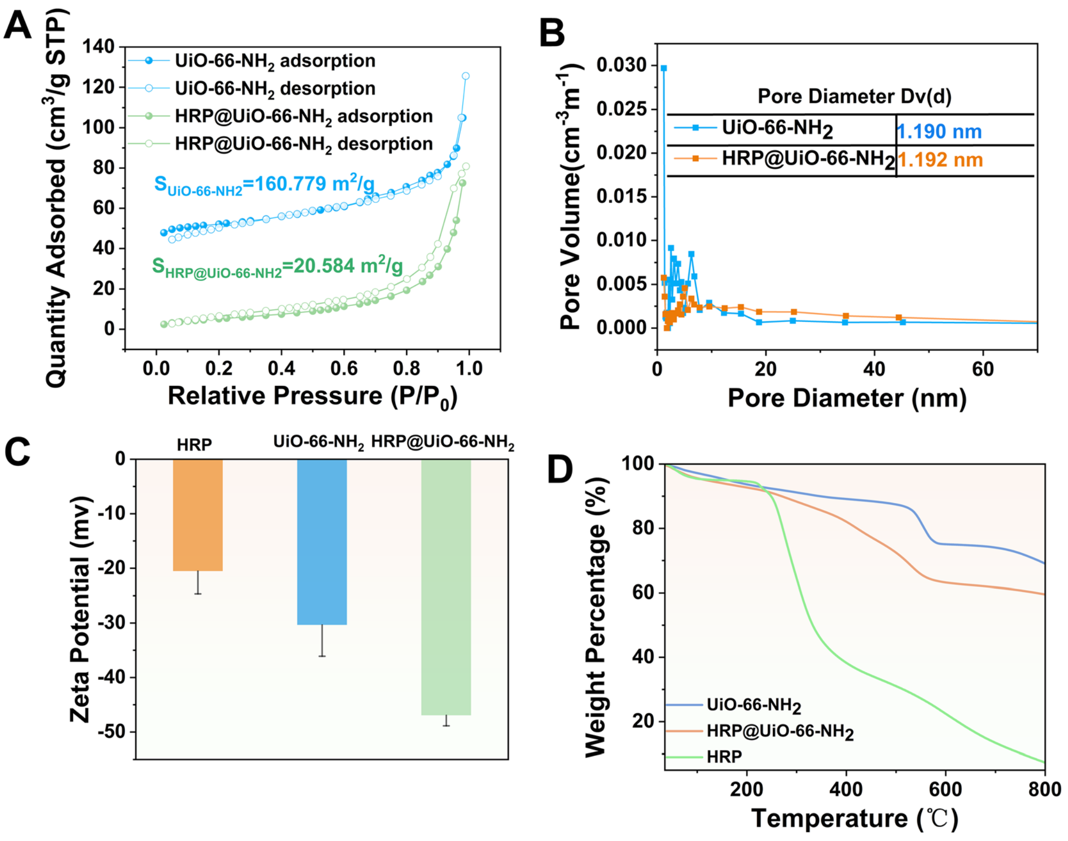

Fig. 3 Mechanism of immobilization. N_2 adsorption–desorption isotherms (A) and DFT pore diameters (B) of UiO-66-NH_2 and HRP@UiO-66-NH_2. (C) Zeta potential comparison of UiO-66-NH_2, HRP, and HRP@UiO-66-NH_2. (D) TGA spectra of UiO-66-NH_2 and HRP@UiO-66-NH_2.

3.2 Evaluation of enzyme loading capacity, immobilization efficiency, and catalytic performance

TMB is frequently employed as a substrate for HRP, reacting chromogenically when oxidized.[48] The enzyme activity of HRP@UiO-66-NH_2 was evaluated by detecting the absorbance of the ox-TMB complex at 652 nm. As depicted in Fig. 4A, UiO-66-NH_2 did not show peroxidase-mimetic catalytic activity; only the combination of HRP@UiO-66-NH_2 and H_2O_2 exhibited absorption at 652 nm, providing evidence of the catalytic capability of the immobilized enzyme derived from bound HRP. The same phenomenon occurred when ABTS and OPD were used as the substrates (Fig. S9†). It is also evident that the catalytic activity of HRP is higher than that of the free HRP after immobilization on the surface of UiO-66-NH_2. This is mainly due to the fact that the nanoscale matrix reduced the mass transfer distance, and the porous structure of UiO-66-NH_2 had a certain aggregation ability to the substrate, thus reducing the mass transfer resistance.[49] Achieving a high enzyme load is also a challenge for immobilized enzyme-mediated signal amplification strategies. According to the calibration curve drawn by Bradford (Fig. S10†), the calculated immobilization efficiency was 91.26% and the enzyme loading was 273.8 mg g^{-1}, respectively.

Detailed comparisons of the catalytic efficiencies of both immobilized and free enzymes were conducted by analyzing their kinetic behaviors, fitting the kinetic parameters (V_{max} and K_m) for the immobilized enzymes. Prior to this phase, parameters for the reaction such as pH, temperature, and duration were adjusted to optimal levels. As shown in Fig. S11,† the absorption value of ox-TMB was maximum at pH = 4.4; however, the ox-TMB absorbance value at pH = 4.0 was approximately the same as that at pH = 4.4. Due to the potent oxidizing nature of nitrite, which necessitates an acidic setting, further studies were conducted at a pH of 4.0. Moreover, it can be observed from Fig. S12,† that during the process of TMB catalyzed by HRP@UiO-66-NH_2, the absorbance value increased rapidly in the first 20 min, especially in the first 15 min, and the absorbance value increased slowly after 20 min. Subsequently, experiments conducted at both 20 °C and 30 °C demonstrated negligible differences in outcomes, and thus room temperature was selected for the reaction to simplify the experimental process (Fig. S13†).

As shown in Fig. 4B, C and Table S1,† the K_M of the immobilized enzyme for TMB and H_2O_2 was 0.23 mM, and 1.00 mM, respectively, both lower than that of free HRP. The results showed that the immobilized enzyme had a high affinity for TMB,[50] which may be due to the ligand of UiO-66-NH_2 containing an intact aromatic structure and carboxyl groups, which can provide sufficient binding sites for the substrate and further promote the catalytic reaction.

Temperature and pH are key factors that could affect the activity of enzymes. Consequently, an investigation was conducted to determine the pH and temperature tolerance of both immobilized and free enzymes. As depicted in Fig. 4D, HRP@UiO-66-NH_2 demonstrated superior stability throughout

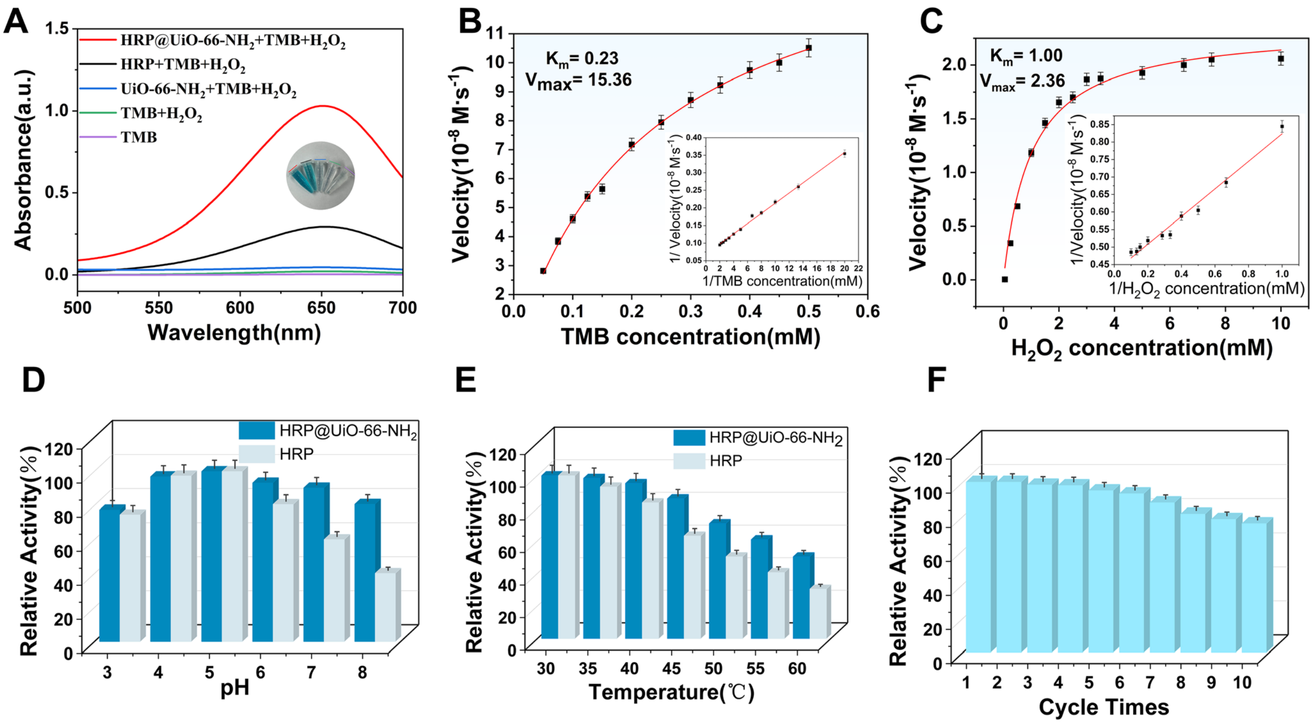

Fig. 4 Enzymatic properties. (A) UV–vis spectra of different systems. Michaelis–Menten curves for the reaction between (B) HRP@UiO-66-NH_2 and TMB and (C) between HRP@UiO-66-NH_2 and H_2O_2 (inset: corresponding Lineweaver–Burk curve of HRP@UiO-66-NH_2). (D) pH stability and (E) temperature stability of free HRP and HRP@UiO-66-NH_2. (F) Cycling stability of HRP@UiO-66-NH_2.

a broader pH variety. In the pH range from 3 to 5, both the immobilized enzyme and the free enzyme exhibited significant catalytic activity. However, when the pH increased, the catalytic activity of the free enzyme experienced a substantial decline compared to the immobilized enzyme. In particular, at a pH value of 8, HRP@UiO-66-NH_2 experienced a fall in activity of approximately 20%, whereas the free HRP suffered a loss of over 60% of its activity. With an increase in temperature, the catalytic activities of both enzymes were affected. When the temperature was increased to 60 °C, the immobilized enzyme retained 50% of its original activity, whereas the free enzyme was only 30% active (Fig. 4E). The ordered porosity and stable environment created by MOFs help shield the enzyme from environmental stressors, such as temperature fluctuations, pH changes, and dehydration. This protection is crucial for enzymes, which are prone to conformational changes or denaturation under harsh conditions. The MOF structure, therefore, acts as a physical barrier, reducing enzyme exposure to such factors and improving its tolerance. Reusability is one of the most prominent advantages of immobilized enzymes. According to Fig. 4F, 75% of the catalytic activity was retained after 10 cycles, demonstrating excellent recyclability compared to previous studies (Table S2†). This may be due to partial enzyme loss during centrifugation. Finally, the immobilized enzyme was stored in a refrigerator at 4 °C and its catalytic activity was measured at regular intervals. Fig. S13† shows that the immobilized enzyme retained 80% of its activity after 90 days. In summary, by fixing the enzyme on UiO-66-NH_2, its tolerance to harsh environments is significantly improved, the problem of free enzymes being difficult to recover is solved, and the cost of industrial application of enzymes is reduced.

3.3 Colorimetric and fluorometric multi-mode detection of nitrite

In the previous study, the HRP@UiO-66-NH_2 system exhibited a blue color owing to the catalysis of TMB to produce ox-TMB. However, in acidic environments, nitrites demonstrate strong oxidation capacity.[51] Therefore, when nitrite is introduced, the nitrite acts as a catalyst, causing the TMB intermediates to lose further electrons and be oxidized, producing a yellow color.[52] Additionally, under such circumstances, nitrite is capable of diazotizing the aromatic primary amine group of the TMB complex to yield yellow diazotized TMB. Notably, both yellow ox-TMB and diazotized TMB produce a strong absorption peak at 445 nm.[53]

In addition to the color change in the solution, the fluorescence of HRP@UiO-66-NH_2 was suppressed in the presence of NO_2^-. Moreover, it was discovered that the fluorescence of the solution bursts remained consistent, regardless of whether TMB was present or not (Fig. S15†). It was hypothesized that the fluorescence burst of HRP@UiO-66-NH_2 was due to the diazotization reaction of NO_2^- with the amino group of UiO-66-NH_2.[54] To test this hypothesis, the Griess test was conducted to confirm the occurrence of diazotization. As shown in Fig. 5B, HRP@UiO-66-NH_2 did not cause a color change in the absence of NO_2^-. After the addition of NO_2^- in the presence of (*N*-(1-naphthalene–naphthalene) ethylenediamine hydrochloride) Griess reagent, a distinct purple color was observed. Moreover, the color of the solution gradually changed to dark purple as the concentration of NO_2^- increased, whereas the absorption at 550 nm gradually increased. Fig. 5C demonstrates the effect of NO_2^- on the fluorescence decay curve of HRP@UiO-66-NH_2. According to the results in Fig. 5C, after reacting with NO_2^-, the fluorescence lifetime of HRP@UiO-66-NH_2 decays from 50.91 ns to 45.67 ns, indicating the occurrence of dynamic quenching. Based on the above arguments, changes in the visual color and fluorescence intensity provide a viable method for the development of colorimetric/fluorescence dual-mode sensors for nitrite analysis.

To achieve the best detection effect, the detection conditions were optimized. According to Fig. S17,† the ratio of absorbance at 445 nm to 652 nm stabilized after 15 minutes of reaction with NO_2^- in the detection system. Therefore, UV absorption and fluorescence spectra were recorded 15 minutes after introducing NO_2^- into the detection system.

As depicted in Fig. 5A, the colorimetric method was initially used to detect NO_2^-, revealing that as the NO_2^- concentration rose, the solution's color transitioned from blue to green and eventually to yellow. At the same time, the absorbance at 652 nm decreased and the absorption peak at 445 nm increased (Fig. 5D). A strong linear correlation was observed between the logarithm of NO_2^- concentration and the absorbance ratio (A_{652}/A_{445}) within the 10–400 μM range, described by the equation $y = -3.11x + 8.09$ ($R^2 = 0.99$) (Fig. 5E). The detection limit (LOD) was calculated to be 0.21 μM using the formula $3\sigma/s$ (where σ represents the standard deviation of the blank measurements and s denotes the slope of the calibration curve).

Subsequently, NO_2^- in the solution was measured under the same conditions using the fluorescence mode. According to Fig. 5A and G, the sensor's fluorescence intensity progressively diminished as the NO_2^- concentration rose. The linear fitting equation was $y = -1304.42x + 3431.98$ ($R^2 = 0.98$) in the range of 5–500 μM with a detection limit of 0.19 μM (Fig. 5H). Similarly, the response of UiO-66-NH_2 to nitrite alone was analyzed. The fluorescence of UiO-66-NH_2 was quenched by NO_2 under the same conditions, showing a linear correlation in the 100–800 μM range (Fig. S18†), but this did not meet the detection limit for nitrite.

Furthermore, the sensor's stability was assessed by storing it at 4 °C for a duration of 30 days, during which no notable alterations in absorbance values and fluorescence intensity were observed, as illustrated in Fig. S19.† The dual-mode colorimetric/fluorescence sensing strategy's selectivity and resistance to interference were evaluated by measuring NO_2^- levels both in the presence and absence of various interfering substances. Metal and inorganic ions, among other common substances, were found to have an insignificant impact on NO_2^- detection (Fig. 5F and I). This indicated that the constructed colorimetric/fluorescence dual-mode sensor had good stability, selectivity, and anti-interference properties.

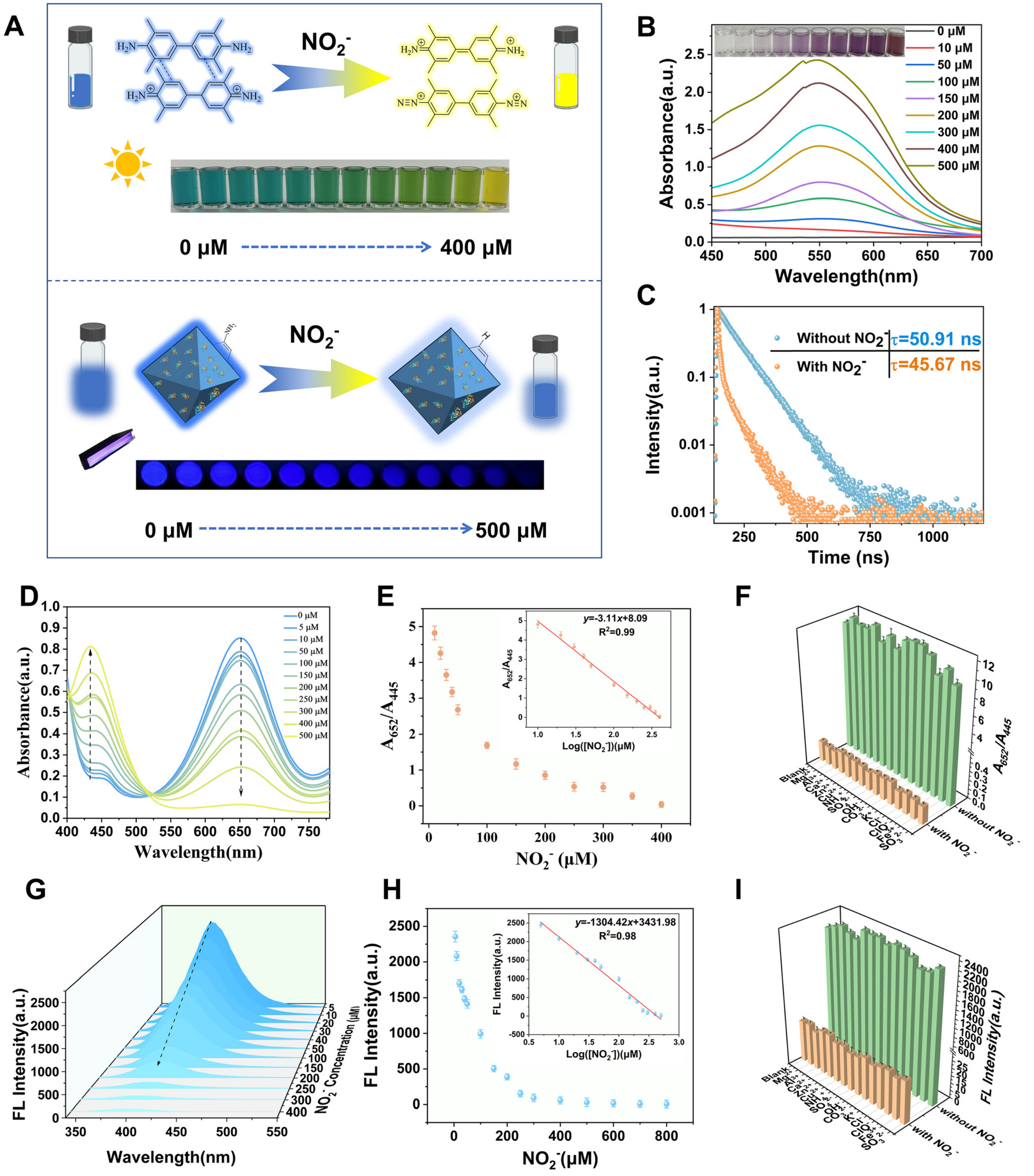

Fig. 5 Colorimetric and fluorescent detection of NO_2^-. (A) Schematic illustration of the detection mechanism of the colorimetric/fluorometric sensor. (B) Griess test results: UV–vis response of HRP@UiO-66-NH_2 (550 nm) to various NO_2^- concentrations with the addition of *N*-(1-naphthalene) ethylenediamine dihydrochloride (inset: photographs under natural light). (C) Fluorescence lifetimes of HRP@UiO-66-NH_2 in the presence and absence of NO_2^-. (D) UV–vis absorption patterns and (G) fluorescence spectra of HRP@UiO-66-NH_2 + TMB + H_2O_2 + NO_2^- with NO_2^- at various levels. (E) Relationship between the A_{652}/A_{445} value and the concentration of NO_2^- (inset: linear relationship between the absorbance value A_{652}/A_{445} and the logarithm of NO_2^- concentration). (H) Relationship between fluorescence intensity (*F*410) and the NO_2^- concentration of NO_2^- (inset: linear relationship between fluorescence intensity (*F*410) and NO_2^- concentration). (F) Colorimetric and (I) fluorometric responses of the method toward various species, respectively.

In comparison to the nitrite detection methods listed in Table S3,† the newly developed dual-mode colorimetric/fluorescence technique described here exhibited enhanced sensitivity, a wide detection range, and a low detection limit, proving its effectiveness for regular quantitative analysis. Furthermore, the fluorescence mode reduces matrix interference, and the nitrite test established in this study can be used to directly detect nitrite with the naked eye. In addition, cross-verification of the results from both modes enhanced the overall accuracy of the detection process.

3.4 Application in real samples

Aiming to assess the practicality of the approach devised in this research, it was employed to detect the concentration of nitrite in lake water, sausages, and pickles. The recoveries were calculated using standard addition, and the results are shown in Table S4.† The recoveries of the colorimetric and fluorescence methods were 89.31%–101.96% and 89.24%–103.62%, respectively. These results demonstrate that the method is both stable and practical for analyzing real samples. The HRP@UiO-66-NH_2-based sensor was highly practical for nitrite detection in complex matrices.

3.5 Development of the portable nitrite gelatin kit

To further exploit the practical application potential of the HRP@UiO-66-NH_2 nitrite-sensing platform, a portable hydrogel kit was developed for the rapid on-site detection of nitrite. Gelatin originates from the partial hydrolysis of collagen found in animal bones and leather, forming a hydrophilic macromolecular colloid. Due to its biocompatibility, non-toxicity, and degradability, gelatin finds extensive applications in both the medical and food industries.[55] In addition, gelatin is rich in carboxyl, amino, and other groups, which promote the chemical reaction between gelatin and other substances, such as HRP@UiO-66-NH_2, and stable hydrogels can be formed without other steps.[56,57] Hence, gelatin was chosen as the substrate to prepare the stimulus-responsive hydrogel kit in this study. In addition, the color change induced by NO_2^- was confirmed by the chromaticity coordinates of the International Commission on Illumination (CIE) (Fig. 6C). An increase in NO_2^- concentration results in a color transition from blue to green and eventually yellow, as depicted in the CIE chromaticity diagram. This color change serves as the foundation for visually detecting NO_2^- with portable equipment.

First, gelatin was heated to form a colloid and then allowed to cool. After a 20-minute reaction period, a solution containing HRP@UiO-66-NH_2, TMB, and H_2O_2 was introduced into the gelatin mixture. An HRP@UiO-66-NH_2-based nitrite hydrogel sensing array was constructed using a 96-well plate as a container. Then, it is combined with a smartphone to develop a visual detection method to meet the needs of rapid on-site detection (Fig. 6A).

As shown in Fig. 6A, the color of the prepared hydrogel matrix changed with an increase in NO_2^- concentration. This color change showed a trend consistent with the change in the liquid system, which demonstrated that the presence of gelatin

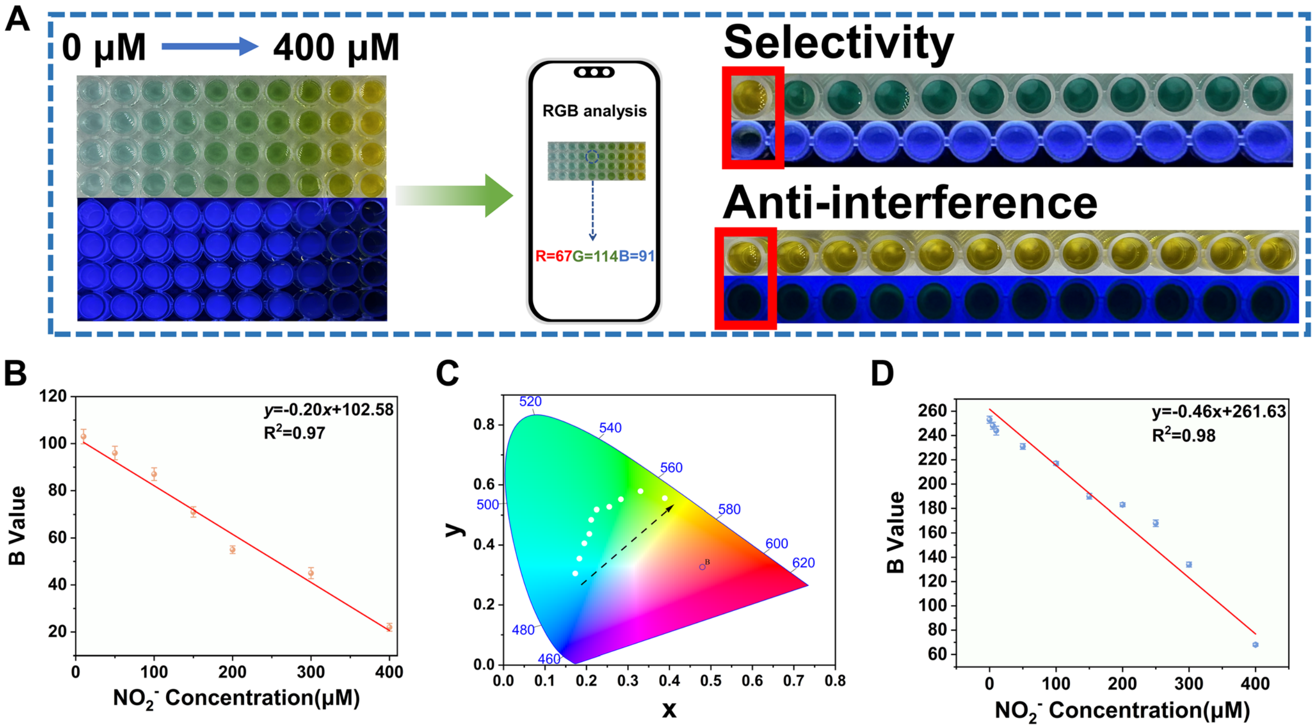

Fig. 6 Gelatin kit development. (A) Photographs of different concentrations of NO_2^- in the kit as well as the selectivity and immunity of the kit under sunlight and UV light. (B) Relationship between the concentration of NO_2^- and the B value (under sunlight). (C) CIE chromaticity coordinates of the kit for NO_2^- at various concentrations. (D) Relationship between the concentration of NO_2^- and the B value (under UV light).

had no impact on the reaction between NO_2^- and TMB or between NO_2^- and HRP@UiO-66-NH_2. Following the colorimetric reaction, a smartphone was used to capture an image of the kit, and the RGB values of the resulting image were subsequently analyzed using an image processing program. Surprisingly, the B value exhibited a strong linear correlation with NO_2^- concentrations between 10 and 400 μM, described by the equation $y = -0.20x + 102.58$ ($R^2 = 0.97$) (Fig. 6B). Photographs under UV light were processed using the same program with higher sensitivity compared to the colorimetric mode, enabling the detection of low concentrations of nitrite. A good linearity was obtained in the range of 0–400 μM with the linear equation $y = -0.46x + 261.63$ ($R^2 = 0.98$) (Fig. 6D).

Selective recognition and anti-interference are important indicators for evaluating the usefulness of the kit. Consequently, the earlier discussed interfering substances were added to the hydrogel kit to mimic actual conditions. Fig. 6C and D show the change in color of the nitrite kit. In the presence of nitrite alone, the color of the kit changed obviously and the fluorescence burst was significant. In the presence of nitrite along with other interfering substances, a noticeable color shift was easily discernible to the naked eye. This demonstrated that the designed kit possessed strong selectivity and resistance to interference. To sum up, the hydrogel kit based on the HRP@UiO-66-NH_2 colorimetric/fluorescence dual-mode sensor is suitable for visual detection and semi-quantitative analysis of nitrite in on-site applications.

4. Conclusions

In conclusion, we synthesized HRP@UiO-66-NH_2 and created a dual-mode sensing platform utilizing both colorimetric and fluorescence methods for detecting nitrite. By immobilizing HRP on UiO-66-NH_2, the catalytic activity was significantly enhanced and the enzyme could be reused, which greatly reduced the cost. Furthermore, a sensing platform for nitrite was developed by merging the catalytic activity of enzymes with the fluorescence characteristics of UiO-66-NH_2. TMB was chosen as the catalytic substrate, and the platform utilized the principle that nitrite can undergo a diazotization reaction with primary amine groups. The dual-mode platform exhibited exceptional sensitivity, stability, and selectivity, with limits of detection of 0.21 μM (in colorimetric mode) and 0.19 μM (in fluorescence mode), respectively. This approach has proven effective for accurately detecting nitrite in actual samples, demonstrating significant potential for practical applications. Moreover, a compact dual-mode hydrogel kit was developed and integrated with a smartphone for *in situ* nitrite detection. This approach showed significant promise for visual detection of nitrite in both food and environmental samples. It also expands the applicability of enzyme-based sensors, providing a versatile tool for sensitive, real-time detection, especially in food safety and environmental monitoring.

Author contributions

Zuyao Fu: writing – review & editing, writing – original draft, methodology, and data curation. Lingfeng Yang: data curation, methodology, and visualization. Zhaoyang Ding: writing – review & editing, supervision, methodology, conceptualization, and funding acquisition. Jing Xie: supervision and project administration.

Data availability

The data supporting this article have been included as part of the ESI.†

Conflicts of interest

The authors declared that they have no conflicts of interest in this work.

Acknowledgements

We would like to sincerely thank the National Key R&D Program of China (Grant No. 2023YFD2401405) and the earmarked fund for CARS-47 for the financial support of our work.

References

1 U. T. Bornscheuer, G. W. Huisman, R. J. Kazlauskas, S. Lutz, J. C. Moore and K. Robins, *Nature*, 2012, **485**, 185–194.
2 H. Wang, Z. Zhao, Y. Liu, C. Shao, F. Bian and Y. Zhao, *Sci. Adv.*, 2018, **4**, eaat2816.
3 R. Breslow, *Acc. Chem. Res.*, 1995, **28**, 146–153.
4 X. Zhang, D. Qiu, J. Chen, Y. Zhang, J. Wang, D. Chen, Y. Liu, M. Cheng, D. Monchaud, J.-L. Mergny, H. Ju and J. Zhou, *J. Am. Chem. Soc.*, 2023, **145**, 4517–4526.
5 Z.-W. Zhou, C.-X. Cai, X. Xing, J. Li, Z.-E. Hu, Z.-B. Xie, N. Wang and X.-Q. Yu, *Biotechnol. Biofuels*, 2021, **14**, 156.
6 S. Cantone, V. Ferrario, L. Corici, C. Ebert, D. Fattor, P. Spizzo and L. Gardossi, *Chem. Soc. Rev.*, 2013, **42**, 6262.
7 L. Wang, Y. Li, X. Du, J. Wu, Z. Zhang, H. Jin, H. Liang and D. Gao, *J. Hazard. Mater.*, 2023, **454**, 131505.
8 Y. Li, L. Yan, G. Liu, H. Chen, H. Zhao, L. Wang, J. Gao, Y. Liu, X. Zheng and Y. Jiang, *Chem. Eng. J.*, 2023, **466**, 143198.
9 X. Yan, K. Chen, H. Jia, Q. Zhao, G. Du, Q. Guo, H. Chen, Y. Yuan and T. Yue, *Food Chem.*, 2024, **431**, 137172.
10 C. S. Thomas, M. J. Glassman and B. D. Olsen, *ACS Nano*, 2011, **5**, 5697–5707.
11 R. Ren, G. Cai, Z. Yu, Y. Zeng and D. Tang, *Anal. Chem.*, 2018, **90**, 11099–11105.

12 X. Dou, K. Sun, H. Chen, Y. Jiang, L. Wu, J. Mei, Z. Ding and J. Xie, *Antibiotics*, 2021, **10**, 358.

13 X. Dou, G. Wu, Z. Ding and J. Xie, *Food Chem.*, 2023, **416**, 135805.

14 T. J. Pisklak, M. Macías, D. H. Coutinho, R. S. Huang and K. J. Balkus, *Top. Catal.*, 2006, **38**, 269–278.

15 N. Motamedi, M. Barani, A. Lohrasbi-Nejad, M. Mortazavi, A. Riahi-Medvar, R. S. Varma and M. Torkzadeh-Mahani, *Nanomaterials*, 2021, **11**, 1759.

16 F. Hong, L. Ren and Y. Chen, *Chem. Eng. J.*, 2023, **452**, 139149.

17 K. Cheng, F. Svec, Y. Lv and T. Tan, *Small*, 2019, **15**, 1902927.

18 K. Ledezma-Zamora, R. Sánchez-Gutiérrez, A. Ramírez-Leiva and L. Mena-Rivera, *Food Chem.*, 2021, **361**, 130082.

19 M. H. Shakil, A. T. Trisha, M. Rahman, S. Talukdar, R. Kobun, N. Huda and W. Zzaman, *Foods*, 2022, **11**, 3355.

20 C.-Y. Hou, L.-M. Fu, W.-J. Ju and P.-Y. Wu, *Chem. Eng. J.*, 2020, **398**, 125573.

21 G. Berardi, M. Albenzio, R. Marino, T. D'Amore, A. Di Taranto, V. Vita and M. Iammarino, *LWT–Food Sci. Technol.*, 2021, **150**, 112004.

22 M. Rong, D. Wang, Y. Li, Y. Zhang, H. Huang, R. Liu and X. Deng, *J. Anal. Test.*, 2021, **5**, 51–59.

23 M. Iammarino, M. Mangiacotti and A. E. Chiaravalle, *Int. J. Food Sci. Technol.*, 2020, **55**, 1097–1109.

24 S. Deng, X. Bai, Y. Li, B. Wang, B. Kong, Q. Liu and X. Xia, *Meat Sci.*, 2021, **181**, 108604.

25 M. Yu, H. Zhang, Y. Liu, Y. Zhang, M. Shang, L. Wang, Y. Zhuang and X. Lv, *Food Chem.*, 2022, **374**, 131768.

26 Q.-H. Wang, L.-J. Yu, Y. Liu, L. Lin, R. Lu, J. Zhu, L. He and Z.-L. Lu, *Talanta*, 2017, **165**, 709–720.

27 W. L. Daniel, M. S. Han, J.-S. Lee and C. A. Mirkin, *J. Am. Chem. Soc.*, 2009, **131**, 6362–6363.

28 S. Liu, H. Qu, L. Yao, Y. Mao, L. Yan, B. Dong and L. Zheng, *Sens. Actuators, B*, 2023, **397**, 134707.

29 M. Wang, H. Zhu, B. Liu, P. Hu, J. Pan and X. Niu, *ACS Appl. Mater. Interfaces*, 2022, **14**, 44762–44771.

30 X. Yue, L. Fu, C. Wu, C. Hao and Y. Bai, *J. Food Compos. Anal.*, 2025, **139**, 107027.

31 J. Zhang, H. Chen, J. Liu, J. Gui, M. Liu, Y. Zhang and S. Yao, *Talanta*, 2023, **258**, 124458.

32 S. Sh. Mohammad Ameen and K. M. Omer, *Food Chem.*, 2025, **462**, 141027.

33 J. Liu, L. Gong, H. Chen, J. Gui, X. Zhu, M. Liu, Y. Zhang and S. Yao, *ACS Appl. Nano Mater.*, 2023, **6**, 5879–5888.

34 S. Deng, J. Liu, D. Han, X. Yang, H. Liu, C. Zhang and C. Blecker, *J. Hazard. Mater.*, 2024, **463**, 132898.

35 M. Wang, P. Liu, H. Zhu, B. Liu and X. Niu, *Biosensors*, 2021, **11**, 280.

36 J. Juan-Colás, S. Johnson and T. Krauss, *Sensors*, 2017, **17**, 2047.

37 M. Wang, J. Xu, L. Li, H. Shen, Z. Ding and J. Xie, *Food Chem.*, 2024, **440**, 138211.

38 M. M. Bradford, *Anal. Biochem.*, 1976, **72**, 248–254.

39 L. E. Kreno, K. Leong, O. K. Farha, M. Allendorf, R. P. Van Duyne and J. T. Hupp, *Chem. Rev.*, 2012, **112**, 1105–1125.

40 H. Zeng, Z. Yu, L. Shao, X. Li, M. Zhu, Y. Liu, X. Feng and X. Zhu, *Chem. Eng. J.*, 2021, **403**, 126281.

41 Z. Xu, X. Deng, Y. Chen, J. Wen, L. Shi and Z. Bian, *Sol. RRL*, 2021, **5**, 2000416.

42 Z. Sun, Y. Z. Fan, S. Z. Du, Y. Z. Yang, Y. Ling, N. B. Li and H. Q. Luo, *Anal. Chem.*, 2020, **92**, 7273–7281.

43 X. Du, G. Wu, X. Dou, Z. Ding and J. Xie, *Food Chem.*, 2024, **445**, 138700.

44 P. Zhang, Y. Xu, K. Guo, Y. Yin, J. Wang and Y. Zeng, *J. Hazard. Mater.*, 2021, **418**, 126247.

45 A. S. Eltaweil, H. M. Elshishini, Z. F. Ghatass and G. M. Elsubruiti, *Powder Technol.*, 2021, **379**, 407–416.

46 J. Wu, J. Han, Y. Mao, L. Wang, Y. Wang, Y. Li and Y. Wang, *Sep. Purif. Technol.*, 2022, **297**, 121505.

47 Y. Zheng, S. Zhang, J. Guo, R. Shi, J. Yu, K. Li, N. Li, Z. Zhang and Y. Chen, *Angew. Chem., Int. Ed.*, 2022, **61**, e202208744.

48 X. Zhang, Q. Yang, Y. Lang, X. Jiang and P. Wu, *Anal. Chem.*, 2020, **92**, 12400–12406.

49 F. Lyu, Y. Zhang, R. N. Zare, J. Ge and Z. Liu, *Nano Lett.*, 2014, **14**, 5761–5765.

50 C. Song, W. Ding, W. Zhao, H. Liu, J. Wang, Y. Yao and C. Yao, *Biosens. Bioelectron.*, 2020, **151**, 111983.

51 J. Zhang, H. Chen, J. Liu, J. Gui, M. Liu, Y. Zhang and S. Yao, *Talanta*, 2023, **258**, 124458.

52 Z. Ma, J. Li, X. Hu, Z. Cai and X. Dou, *Adv. Sci.*, 2020, **7**, 2002991.

53 L. Tian, Z. Huang, X. Lu, T. Wang, W. Cheng, H. Yang, T. Huang, T. Li and Z. Li, *Inorg. Chem.*, 2023, **62**, 1659–1666.

54 M. Liang, Y. Gao, X. Sun, R.-M. Kong, L. Xia and F. Qu, *J. Hazard. Mater.*, 2024, **469**, 134021.

55 R. E. Abou-Zeid, N. S. Awwad, S. Nabil, A. Salama and M. A. Youssef, *Int. J. Biol. Macromol.*, 2019, **141**, 1280–1286.

56 W. Yang, J. Wang, Y. Han, X. Luo, W. Tang, T. Yue and Z. Li, *Food Control*, 2021, **130**, 108409.

57 L. K. Njaramba, M. Kim, Y. Yea, Y. Yoon and C. M. Park, *Chem. Eng. J.*, 2023, **452**, 139426.